Journal of Astronomical Telescopes, Instruments, and Systems

AstronomicalTelescopes.SPIEDigitalLibrary.org

Phase diversity technique with sparse regularization in liquid crystal adaptive optics system

Daosheng Wu
Chengliang Yang
Peiguang Zhang
Zihao Xu
Huanyu Xu
Xingyun Zhang
Zhaoliang Cao
Quanquan Mu
Li Xuan

Daosheng Wu, Chengliang Yang, Peiguang Zhang, Zihao Xu, Huanyu Xu, Xingyun Zhang, Zhaoliang Cao, Quanquan Mu, Li Xuan, "Phase diversity technique with sparse regularization in liquid crystal adaptive optics system," *J. Astron. Telesc. Instrum. Syst.* **4**(4), 049007 (2018), doi: 10.1117/1.JATIS.4.4.049007.

Phase diversity technique with sparse regularization in liquid crystal adaptive optics system

Daosheng Wu,[a,b] Chengliang Yang,[a,*] Peiguang Zhang,[a] Zihao Xu,[a,b] Huanyu Xu,[a] Xingyun Zhang,[a] Zhaoliang Cao,[a] Quanquan Mu,[a,*] and Li Xuan[a]
[a]Chinese Academy of Sciences, Changchun Institute of Optics, Fine Mechanics and Physics, State Key Laboratory of Applied Optics, Changchun, Jilin, China
[b]University of Chinese Academy of Sciences, Beijing, China

Abstract. Phase diversity (PD) technique is an effective method for wavefront sensing and image restoration in adaptive optics (AO). Classical PD with Tikhonov regularization can achieve proper wavefront estimation but constantly results in overly smooth images. Nonlocal centralized sparse representation (NCSR) based on nonlocal self-similarity and the sparsity model is combined with PD to obtain high-resolution images. The proposed method contains two steps: the first step is obtaining wavefront from ordinary PD with Tikhonov regularization, and the second step is deblurring the image with NCSR other than Tikhonov regularization. Numerical simulations show that the peak signal-to-noise ratios and structural similarity index metrics of deblurred images by the proposed method are higher than those by the traditional method. This work also studies the influence of weak noise. Initially, the proposed method is applied to a liquid crystal AO system, where the highest spatial resolutions that can be clearly distinguished are 1.59× diffraction limitation with AO on, 1.41× diffraction limitation with traditional PD, and 1.26× diffraction limitation with the proposed method. The proposed approach can be widely used for AO postprocessing in ground-based telescopes, fluorescence microscopes, and other applications. [DOI: 10.1117/1.JATIS.4.4.049007]

Keywords: phase diversity; sparse regularization; image restoration; liquid crystal; adaptive optics.

Paper 18041 received Jun. 3, 2018; accepted for publication Nov. 26, 2018; published online Dec. 17, 2018.

1 Introduction

Images received by ground-based telescopes are always degraded by atmosphere turbulence, and such degradation is more severe for images received by larger aperture telescopes. Adaptive optics (AO) is an effective tool for reducing aberrations and improving image resolution.[1,2] However, some aberrations still blur the images even after AO. Phase diversity (PD) technique, which was first proposed by Gonsalves and Chidlaw,[3] is a type of digital postprocessing method to improve image quality. This technique uses a focused image and one or more images with known diversity phase to simultaneously reconstruct the wavefront and restore the image. PD can restore the point source and extended objects and has a simple and easy-to-achieve optical layout.[4,5] At present, PD technique is no longer used just for AO wavefront sensing[3] and image postprocessing,[6,7] but also for optical misalignment sensing in segmented aperture telescopes,[8] sensing of noncommon path aberrations in AO systems,[9] and complex magnitude sensing of laser.[10]

Regularization is necessary in image restoration because it is an ill-posed inverse problem from a mathematical view point. Given that the PD technique retrieves both wavefront and image, all wavefronts and images need to be regularized. Wavefront aberrations are always represented by a combination of Zernike polynomials[11] or other basis functions, which entails implicit regularization. Additionally, when PD is used for sensing wavefront distorted by atmosphere turbulence directly, a statistical prior, i.e., turbulence power spectra based on Kolmogorov theory is used.[12,13] A low-pass filter[14,15] and sieve on the object[16] are early methods for the regularization of an object; later, many scientists began using Tikhonov regularization.[12,17,18] Tikhonov regularization is an effective and robust means of addressing the ill-posed inverse problem.[19] However, it always obtains either overly smooth results or sharp images with amplified noise. Block-matching and 3-D filtering (BM3D) algorithms can reduce noise effectively.[20] Yu et al.[21] combined BM3D algorithms with the PD technique to reduce Poisson noise when the photon count level of images is low. Although their work is meaningful, it is still insufficient because regularization is not just for noise. Sparsity is an important feature of natural images, and it has been successfully introduced in image restoration as a kind of regularization strategy. Combining the BM3D algorithm and sparse representation can result in excellent performance. Nonlocal centralized sparse representation (NCSR) is such an algorithm.[22,23] On the basis of the aforementioned findings, we wonder whether adding NCSR to the PD technique can improve the quality of restored images.

This work proposes an effective method to improve image quality using the PD technique with NCSR. Because the merit function is hard to calculate if Tikhonov regularization is directly replaced by NCSR, and the wavefront restored from ordinary PD is pretty accurate, the method is separated to two steps. First, wavefront is constructed by PD with Tikhonov regularization, then point spread function (PSF) is obtained and deconvolution with NCSR is done. The simulation results show that, for different objects, the peak signal-to-noise ratios (PSNRs) of deblurred images by the traditional method improved by 10 dB, while those by the proposed method

*Address all correspondence to Chengliang Yang, E-mail: ycldahai@ciomp.ac.cn; Quanquan Mu, E-mail: muquanquan@ciomp.ac.cn

2329-4124/2018/$25.00 © 2018 SPIE

improved by ~15 to 20 dB. This study likewise investigates the influence of weak noise and finds that the effects of the proposed method are consistently better than those of the traditional PD with the increase of noise. We initially apply this method to a liquid crystal AO system (LC AOS) to verify its practical performance. We find that the highest spatial resolutions that can be clearly distinguished are 1.59× diffraction limitation with AO on, 1.41× diffraction limitation with traditional PD, and 1.26× diffraction limitation with the proposed method. The experiment and simulation results all show that the proposed method performs better than the traditional PD.

2 PD Theory and the Proposed Method

2.1 *Basic PD Theory*

PD technique requires a focused image and one image with known diversity function. For brevity, diversity function is defocus referred to in the following discussion. This PD can be conducted with a simple optical setup, as shown in Fig. 1.

The focused image can be modeled as

$$g(\mathbf{x}) = f(\mathbf{x}) * h(\mathbf{x}) + n(\mathbf{x}), \tag{1}$$

where * stands for the spatial convolution, $g(\mathbf{x})$ is the focused image, $\mathbf{x}$ is a 2-D spatial coordinate, $f(\mathbf{x})$ is the original object, $n(\mathbf{x})$ is the additive noise, and $h(\mathbf{x})$ is the PSF, which includes aberrations from both optical systems and propagation media, especially for atmosphere turbulence. $h(\mathbf{x})$ can be written as

$$h(\mathbf{x}) = |\mathrm{FT}\{P(\mathbf{x})\exp[i\varphi(\mathbf{x})]\}|^2, \tag{2}$$

where FT[ ] denotes the Fourier transform, $P(\mathbf{x})$ is the pupil transfer function, and $\varphi(\mathbf{x})$ is the unknown distorted phase. We express the phase as the sum of the first n Zernike polynomials:

$$\varphi(\mathbf{x}) = \sum_{i=1}^{n} a_i Z_i(\mathbf{x}), \tag{3}$$

where $Z_i(\mathbf{x})$ is the i'th Zernike polynomial, a_i is the corresponding coefficient. The other image can be similarly written as

$$g_d(\mathbf{x}) = f(\mathbf{x}) * h_d(\mathbf{x}) + n_d(\mathbf{x}), \tag{4}$$

where the subscript d stands for the defocus. $h_d(\mathbf{x})$ can be written as

$$h_d(\mathbf{x}) = |\mathrm{FT}\{P(\mathbf{x})\exp[i(\varphi(\mathbf{x}) + \varphi_d(\mathbf{x}))]\}|^2, \tag{5}$$

where $\varphi_d(\mathbf{x})$ is the known defocus. The merit function is then obtained based on the max likelihood

$$E = \sum_{\mathbf{x}} |g(\mathbf{x}) - f(\mathbf{x}) * h(\mathbf{x})|^2 + |g_d(\mathbf{x}) - f(\mathbf{x}) * h_d(\mathbf{x})|^2 + J(f), \tag{6}$$

where $J(f)$ stands for the regularizing term. For the conventional PD merit function with the first-order Tikhonov regularizing term, $J(f) = \lambda_0 |f(\mathbf{x})|^2$, where λ_0 is the regularization coefficient. From Eq. (6), the functions can be derived in the frequency domain as follows:

$$E = \sum_{\mathbf{u}} \frac{|G(\mathbf{u})H(\mathbf{u}) - G_d(\mathbf{u})H_d(\mathbf{u})|^2}{|H(\mathbf{u})|^2 + |H_d(\mathbf{u})|^2 + \lambda_0}, \tag{7}$$

$$\hat{f}(\mathbf{x}) = \mathrm{FT}^{-1}\left[\frac{H^*(\mathbf{u})G(\mathbf{u}) + H_d^*(\mathbf{u})G_d(\mathbf{u})}{|H(\mathbf{u})|^2 + |H_d(\mathbf{u})|^2 + \lambda_0}\right], \tag{8}$$

where $\mathbf{u}$ is a 2-D spatial frequency coordinate; $\mathrm{FT}^{-1}[\,]$ denotes the inverse Fourier transform; $G(\mathbf{u})$, $H(\mathbf{u})$, $G_d(\mathbf{u})$, and $H_d(\mathbf{u})$ are the Fourier transform of $g(\mathbf{x})$, $h(\mathbf{x})$, $g_d(\mathbf{x})$, and $h_d(\mathbf{x})$, respectively; $H^*(\mathbf{u})$ and $H_d^*(\mathbf{u})$ are the complex conjugates of $H(\mathbf{u})$ and $H_d(\mathbf{u})$, respectively; and $\hat{f}$ is the restored image. Some optimization algorithms can then be used to minimize Eq. (7). The hybrid particle swarm algorithm proposed by Zhang et al.[24] can approach the global minimum for PD with high reliability and accuracy. Thus this optimization algorithm is used in the PD technique.

Tikhonov regularization can effectively retrieve wavefronts robustly with just a proper regularizing coefficient, but the restored images tend to be overly smooth, a problem that has also been discussed in Ref. 23 and 25. Therefore, we want to seek a better regularization method.

2.2 *NCSR Regularization*

The nature of regularization is the mathematical representation of appropriate prior knowledge about an original object. Sparsity is an effective representation in image processing

$$\alpha = \arg\ \min\{\|g - (\Phi \oplus \boldsymbol{\alpha}) * h\|_2^2 + \lambda_1 \|\boldsymbol{\alpha}\|_1\}, \tag{9}$$

where $\boldsymbol{\alpha} = [\alpha_1, \alpha_2, \ldots, \alpha_j]$ is the sparse coefficient vector of object f, and λ_1 is the regularization coefficients

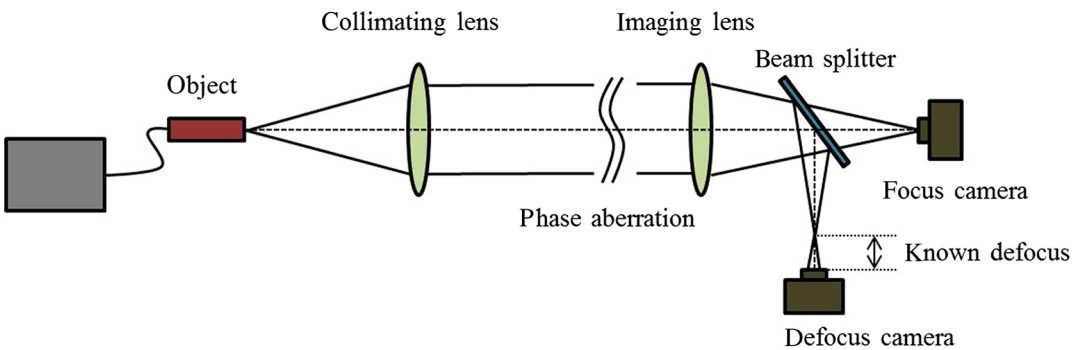

Fig. 1 Optical setup of classic PD technique.

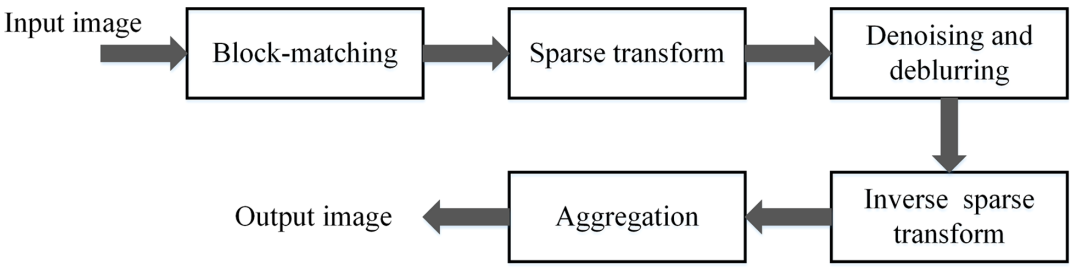

Fig. 2 Flowchart of clustering-based sparse representation algorithms.

$$f = \Phi \oplus \boldsymbol{\alpha}, \tag{10}$$

where Φ is an dictionary, $\oplus$ stands for a sparse coding operator, and most entries of the coding vector $\boldsymbol{\alpha}$ are zero or close to zero, which is guaranteed by the second term. The selection of dictionary Φ can be various. It can be a predefined dictionary or a learned dictionary. Recently, a series of algorithms based on nonlocal self-similarity make obvious improvements on image denoising.[20,22,23] Unlike ordinary sparse regularization, the whole blurred image is separated to a serial of block, which has some similar image patches. Each block has its dictionary, then the sparse coefficient is shrunk to denoise or deblur the image. The scheme is shown as in Fig. 2.

Dong et al.[22] introduced the concept of sparse coding noise based on above and proposed centralized spare representation (CSR). The model of CSR can be written as

$$\boldsymbol{\alpha} = \arg\ \min\{\|g - (\Phi \oplus \boldsymbol{\alpha}) * h\|_2^2 + \lambda_1\|\boldsymbol{\alpha}\|_1 + \gamma\|\boldsymbol{\alpha} - \boldsymbol{\beta}\|_1\}, \tag{11}$$

where γ is the regularization coefficient. The third term is the sparse coding noise, which is the error between estimated sparse coefficients α and real sparse coefficients. $\boldsymbol{\beta}$ denotes some good estimation of α and can be considered as the real sparse coefficients. Normally, $\boldsymbol{\beta}$ can be the mean of α, that is $\boldsymbol{\beta} = E(\boldsymbol{\alpha})$. γ is the regularization coefficients. As mentioned above, each block or cluster has its dictionary. A dictionary of principal component analysis bases is learned here. This actually leads to a very sparse representation for the given block, thus the second term can be removed. That is the nonlocally centralized spare representation (NCSR) model:

$$\alpha = \arg\ \min\{\|g - (\Phi \oplus \boldsymbol{\alpha}) * h\|_2^2 + \gamma\|\boldsymbol{\alpha} - \boldsymbol{\beta}\|_1\}. \tag{12}$$

This model can be derived with maximum *a posterior* (MAP) estimation. Defining $\boldsymbol{\theta} = \boldsymbol{\alpha} - \boldsymbol{\beta}$, then the MAP estimator of $\boldsymbol{\theta}$ can be expressed as follows for a given $\boldsymbol{\beta}$:

$$\begin{aligned}\boldsymbol{\theta} &= \arg\max_{\boldsymbol{\theta}} \log\ P(\boldsymbol{\theta}|g) \\ &= \arg\max_{\boldsymbol{\theta}}\{\log\ P(g|\boldsymbol{\theta}) + \log\ P(\boldsymbol{\theta})\}.\end{aligned} \tag{13}$$

The likelihood term is modeled by the Gaussian distribution

$$\begin{aligned}P(g|\boldsymbol{\theta}) &= P(g|\boldsymbol{\alpha}, \boldsymbol{\beta}) \\ &= \frac{1}{\sqrt{2\pi}\sigma_n}\ \exp\left[-\frac{1}{2\sigma_n^2}\|g - (\Phi \oplus \boldsymbol{\alpha}) * h\|_2^2\right],\end{aligned} \tag{14}$$

where σ_n is the standard deviations of g. According to Ref. 23, assuming that θ follows i.i.d. Laplacian distribution:

$$P(\boldsymbol{\theta}) = \prod_i \prod_j \left\{\frac{1}{\sqrt{2}\sigma_{i,j}}\ \exp\left[-\frac{|\theta_i(j)|}{\sigma_{i,j}}\right]\right\}, \tag{15}$$

where $\theta_i(j)$ is j'th element of θ_i, and $\sigma_{i,j}$ is the standard deviations of $\theta_i(j)$. Thus

$$\boldsymbol{\theta} = \arg\min_{\boldsymbol{\theta}}\left\{\|g - (\Phi \oplus \boldsymbol{\alpha}) * h\|_2^2 + 2\sqrt{2}\sigma_n^2 \sum_i \sum_j \frac{|\theta_i(j)|}{\sigma_{i,j}}\right\}. \tag{16}$$

For a given $\boldsymbol{\beta}$, $\boldsymbol{\alpha}$ can be obtained by

$$\begin{aligned}\boldsymbol{\alpha} = \arg\min_{\boldsymbol{\alpha}}\Bigg\{&\|g - (\Phi \oplus \boldsymbol{\alpha}) * h\|_2^2 \\ &+ 2\sqrt{2}\sigma_n^2 \sum_i \sum_j \frac{1}{\sigma_{i,j}}|\alpha_i(j) - \beta_i(j)|\Bigg\}.\end{aligned} \tag{17}$$

Comparing with Eq. (12), we have

$$\gamma_{i,j} = \frac{2\sqrt{2}\sigma_n^2}{\sigma_{i,j}}. \tag{18}$$

An alternative iterative algorithm[23] can be used to solve Eq. (17).

2.3 *Proposed Method*

If Tikhonov regularization is replaced by NCSR directly, the following merit will be gotten:

$$\begin{aligned}\{\mathbf{a}; \boldsymbol{\alpha}\} = \arg\min_{\mathbf{a},\boldsymbol{\alpha}}\Bigg\{&\|g - (\Phi \oplus \boldsymbol{\alpha}) * h\|_2^2 \\ &+ \|g_d - (\Phi \oplus \boldsymbol{\alpha}) * h_d\|_2^2 + \gamma\sum_j \|\alpha_j - \beta_j\|_1\Bigg\}.\end{aligned} \tag{19}$$

From Eq. (19), explicit object function cannot be gotten, and the solution procedure will be very complex. On the other hand, the accuracy of estimated wavefront is pretty high by ordinary PD with Tikhonov regularization. For convenience of application, the continuous two step method is selected: first, we use the PD technique with Tikhonov regularization to reconstruct the wavefront; second we use NCSR to restore high-resolution images by Eq. (17). The flowchart of proposed method is shown in Fig. 3.

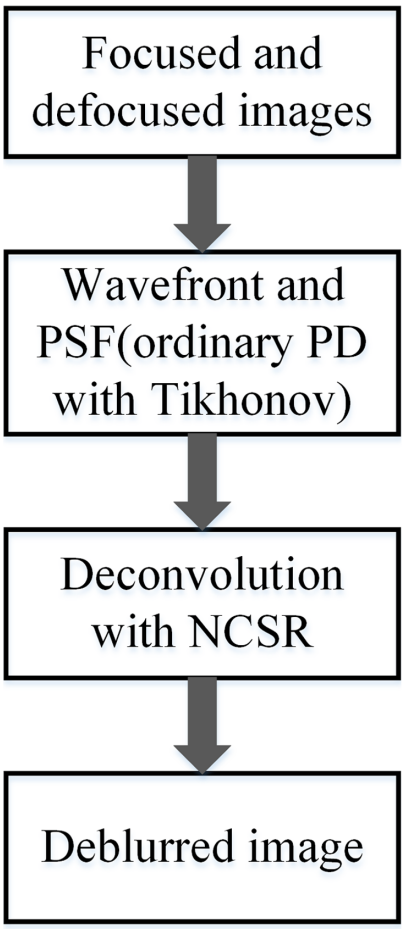

Fig. 3 Flowchart of the proposed method.

3 Numerical Simulations and Experiments

3.1 *Simulations*

A series of numerical simulations is performed to verify the retrieved image quality of the proposed strategy. The focused and defocused images are generated with a known random wavefront based on the above PD theory. Some classical pictures are used as the original objects, as shown in Fig. 4. The known random phase shown in Fig. 5, which is expressed as the first 15 Zernike polynomials, except for piston and tip/tilt. Empirically, the magnitude of the diversity function (i.e., defocus) is 1 wavelength (1λ) peak-to-valley (PV). The scale of the pupil wavefront is indicated by the root mean square (RMS). The RMS of the random wavefront is 0.25λ. The simulations need to satisfy the Nyquist sampling theorem. The values of some parameters are listed in Table 1 and are in agreement with the following experiment.

After simulated imaging in a charge-coupled device (CCD), we add Gaussian noise with 0 mean and $\sigma^2 = 1 \times 10^{-4}$ variance and Poisson noise considering intensity disturbance in an actual experiment. The accuracy of the retrieved phase is measured by the RMS error (RMSE) of wavefront difference $\Delta\varphi$ between the estimated and original phases. RMSE can be calculated as

$$\mathrm{RMSE}(\lambda) = \frac{1}{2\pi}\sqrt{\frac{1}{N_p}\sum_{j=1}^{N_p}[\Delta\varphi(j) - \mathrm{aver}(\Delta\varphi)]^2}, \tag{20}$$

$$\Delta\varphi = \hat{\varphi} - \varphi, \tag{21}$$

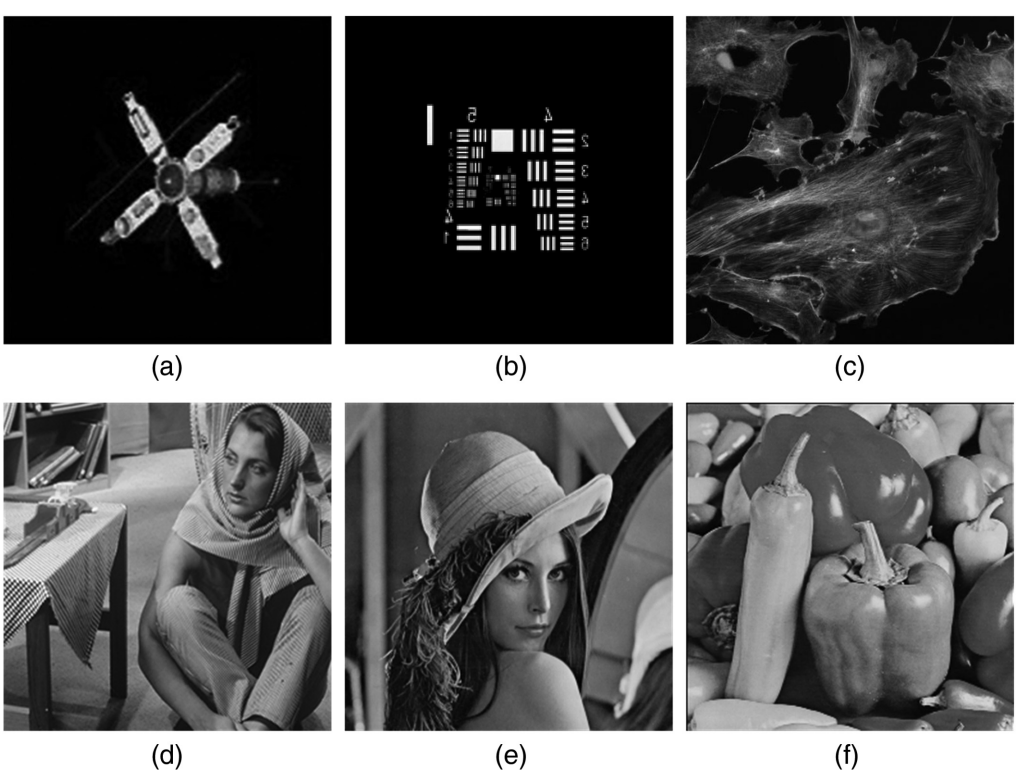

Fig. 4 Original objects: (a) marine satellite, (b) optical resolution test board USAF-1951, (c) Barbara, (d) FluorescentCells (open sample from the software ImageJ), (e) Lena, and (f) Peppers.

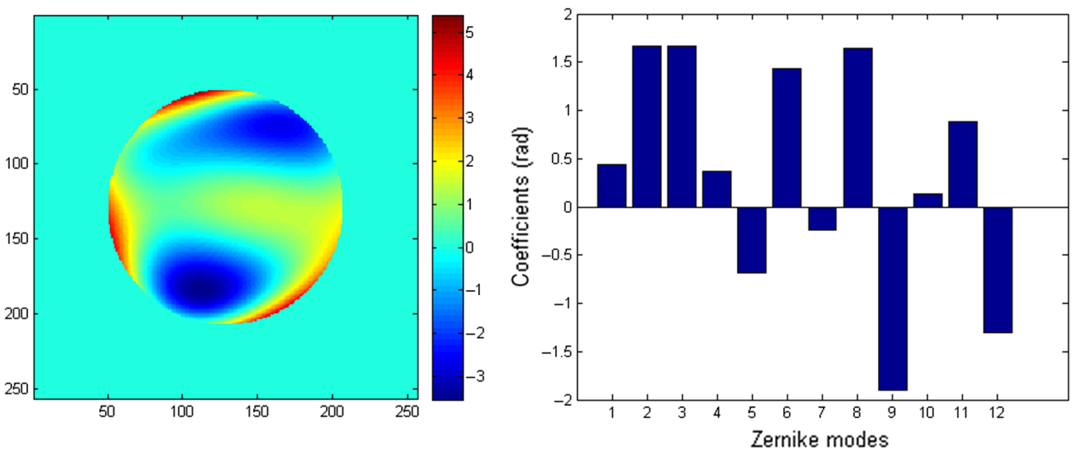

(a) (b)

Fig. 5 Random phase (units: radius): (a) phase image, (b) corresponding coefficients of Zernike polynomials.

Table 1 Values of some parameters in simulation.

Wavelength	780 nm
Diameter of exit pupil	17 mm
Pixel size of CCD	13 μm
Sample pixels	200×200

$$\text{aver}(\Delta\varphi) = \frac{1}{N_p}\sum_{j=1}^{N_p}[\hat{\varphi}(j) - \varphi(j)], \tag{22}$$

where N_p denotes the number of discrete points in the pupil, $\hat{\varphi}$ is the retrieved phase, and aver($\Delta\varphi$) is the mean of the difference between restored wavefront and original wavefront. PSNR and structural similarity index metric (SSIM)[26] are used as assessment standards of the restored image quality

$$\text{PSNR(dB)} = 10\log_{10}\left\{\frac{\max[f(j)]^2}{\frac{1}{N}\sum_{j=1}^{N}[\hat{f}(j) - f(j)]^2}\right\}, \tag{23}$$

where N is the number of pixels in the image. The SSIM is calculated as follows:

$$\text{SSIM}(\hat{f}, f) = \frac{(2\mu_f\mu_{\hat{f}} + c_1)(2\sigma_{f,\hat{f}} + c_2)}{(\mu_f^2 + \mu_{\hat{f}}^2 + c_1)(\sigma_f^2 + \sigma_{\hat{f}}^2 + c_2)}, \tag{24}$$

where μ is the average, σ^2 is the variance, and c_1 and c_2 are the small constants to stabilize the division. Additionally, the quality of blurred image also evaluated by PSNR for comparison:

$$\text{PSNR(dB)} = 10\log_{10}\left\{\frac{\max[f(j)]^2}{\frac{1}{N}\sum_{j=1}^{N}[g(j) - f(j)]^2}\right\}. \tag{25}$$

The RMSEs of the retrieved phase are 0.0122λ, 0.0283λ, 0.0206λ, 0.0149λ, 0.0193λ, and 0.0095λ. Note that although a smaller RMSE is better in theory, these retrieved phases are accurate enough to build good PSFs. Image deblurring with different regularization methods uses the same PSF as well. The NCSR deblurring method is compared with the conventional Tikhonov regularization. The simulated results are presented in Table 2, and some restored images are shown in Figs. 6 and 7. The results show that, for different objects, the PSNRs of deblurred images by the traditional method are

Table 2 PSNRs and SSIMs of blurred images and restored images for different objects.

Objects	Blurred images (dB)	Tikhonov	NCSR
Marine satellite	55.71	67.88 dB/0.9899	79.67 dB/0.9966
USAF-1951	45.69	62.88 dB/0.9724	77.44 dB/0.9946
Barbara	48.43	60.24 dB/0.9801	65.50 dB/0.9896
FluorescentCells	51.49	62.26 dB/0.9822	65.11 dB/0.9860
Lena	48.14	59.25 dB/0.9779	65.01 dB/0.9872
Peppers	47.86	59.80 dB/0.9842	68.82 dB/0.9938

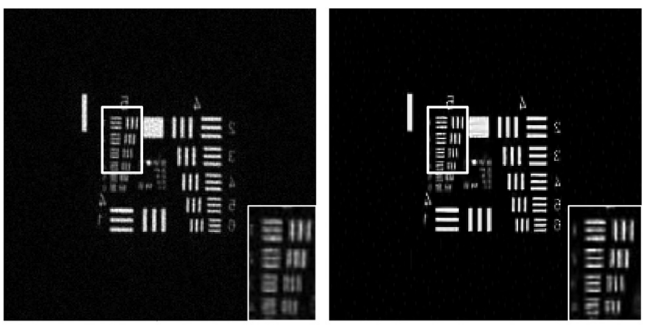

(a) (b)

Fig. 6 Simulated restored results with USAF-1951: (a) restored image with Tikhonov regularization and (b) restored image with NCSR.

(a) (b)

Fig. 7 Simulated restored results with Lena: (a) restored image with Tikhonov regularization and (b) restored image with NCSR.

improved by 10 dB, while those by the proposed method are improved by ∼15 to 20 dB. The SSIMs of the latter are also higher than those of the former. For USAF-1951 in Fig. 6, because of the original image's binary value, the improved PSNR is around 17 dB by the traditional method, while that by the proposed method is ∼32 dB. Furthermore, the quality improvement of the restored image is mainly reflected in the noise reduction. In Fig. 7 (Lena), there are sharper edges and more details restored by NCSR than by the traditional Tikhonov regularization.

We also carried out simulations in different noise levels with USAF-1951 because noise is the main reason for the instability in image restoration. The results are shown in Table 3, which reveals that even when the noise level is low, the quality of restored images falls sharply with the increase of noise. A comparison of the images in Fig. 8 with those in Fig. 6 indicates that the restored images have considerable noise for both methods. However, the effect of NCSR is better than that of Tikhonov regularization. The PSNRs of restored images by Tikhonov regularization decrease from 62.88 to 51.70 dB, and the SSIMs decrease from 0.9724 to 0.9367, whereas the PSNRs of restored images by NCSR decrease from 77.44 to 58.14 dB, and the SSIMs decrease from 0.9946 to 0.9646. In summary, the quality of restored images by the proposed method is always higher than that by the traditional PD.

Table 3 PSNRs and SSIMs of blurred images and restored images for different noise levels.

σ/noisy PSNR	Blurred images (dB)	Tikhonov	NCSR
0.01/91.69 dB	45.69	62.88 dB/0.9724	77.44 dB/0.9946
0.02/77.43 dB	45.57	56.33 dB/0.9604	68.67 dB/0.9868
0.03/70.33 dB	45.34	54.14 dB/0.9437	62.62 dB/0.9773
0.04/64.59 dB	44.95	51.70 dB/0.9367	58.14 dB/0.9646

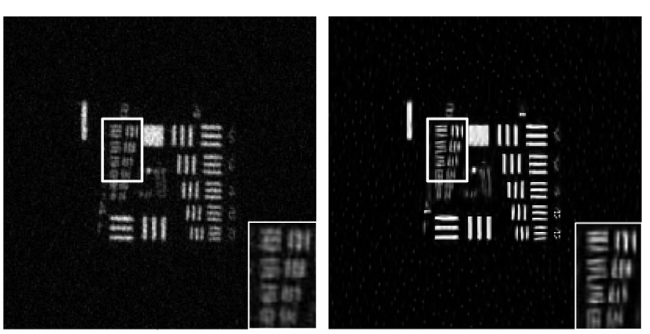

(a) (b)

Fig. 8 Simulated restored results with USAF-1951 under $\sigma = 0.03$: (a) restored image with Tikhonov regularization and (b) restored image with NCSR.

3.2 *Experiments*

In this section, the PD technique with NCSR is initially employed in the LC AOS. Xu et al.[27] proposed a high-resolution imaging approach by applying the PD technique to the open-loop LC AOS. The optical layout of LC AOS is shown in Fig. 9, and a photograph of the experimental setup is shown in Fig. 10. In the experiment, we use the optical resolution test board USAF-1951 illuminated by a white light as the extended object. L1 is the collimating lens to make the light similar to a plane wave. The light then goes through a turbulence phase screen (Lexitek, r_0 : 1.08 mm), a stop to restrict the beam aperture, a tip/tilt mirror to correct the tip/tilt of the phase distortion, a long wavelength pass filter, and optical wave whose wavelength is shorter than 700 nm is reflected to the Shack–Hartmann wavefront sensor. The long wave band from 700 to 900 nm will transmit to the wavefront-correction branch. Given that LC-SLM is useful for polarized waves, two LC-SLMs are used to correct two beams whose polarization directions are perpendicular to each other. Meanwhile, any specific and known PD can be added in one LC-SLM. Here the diversity function is defocus with 0.4λ PV. The LC-SLMs we use both have 256×256 pixels. One corrected beam and another with a known defocus will be imaged in two separate areas in the CCD. Next, PD and NCSR algorithm are used to retrieve residual aberration and restore the image with higher resolution. As the LC AOS is an open-loop system, the residual aberration cannot be obtained after AO correction, and the wavefront retrieved by PD is not displayed. The only measurement is the quality of the deblurred image.

The experimental results are shown in Figs. 11 and 12. Figures 11(a) and 11(b) show the focused images before and after AO, and Fig. 11(c) shows the defocused image used for PD. The resolution of the images obviously improved after AO. Figure 12(a) shows the focused image recorded by CCD with AO on; because of the aperture limitation of the fiber source in LC AOS, what we can see are the line pairs in the fifth group. In this group, even the first element is ambiguous and barely distinguishable. The corresponding spatial resolution is 32.00 lp/mm, which is equivalent to 1.59× diffraction limitation, and residual aberration still occurs. The focused and defocused images are obtained simultaneously on the CCD. Figure 12(b) shows the deblurred image by PD with classical Tikhonov regularization. Compared to Fig. 12(a), the resolution in Fig. 12(b) is improved, and the fifth-group second element whose spatial resolution is 1.41× diffraction limitation (35.92 lp/mm) can be seen clearly. However, the image is filled with noise. Figure 12(c) shows the deblurred image by PD with NCSR. The noise is obviously reduced and the resolution has further improvement. We can clearly see that the third element of the fifth group has a spatial resolution that is 1.26× diffraction

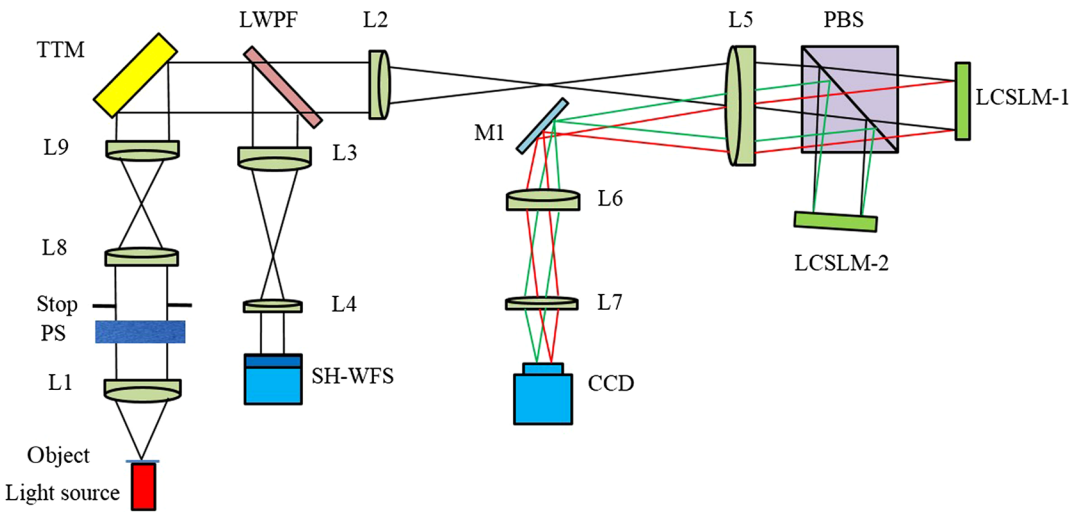

Fig. 9 LC AOS optical layout with PD. L1, L2, L3, L4, L5, L6, L7, L8, and L9 are lenses, object is test chart, PS stands for phase screen, PBS is polarized beam splitter, and M1 is mirror.

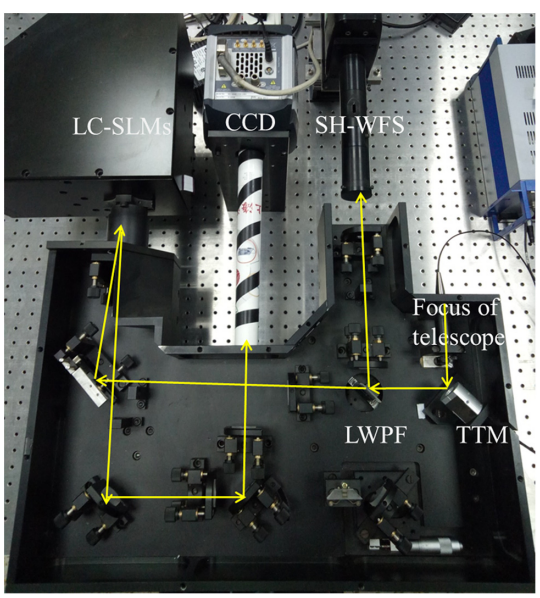

Fig. 10 Photo of LC AOS experimental setup.

limitation (40.32 lp/mm). Partial images in white block are selected to compute the SSIMs, the values of which are 0.0971, 0.2893, and 0.4400, respectively. Thus the proposed approach can obtain finer details and higher spatial resolution than the traditional PD.

4 Conclusion

In this study, we proposed an effective image deblurring method using the PD technique with NCSR and apply it initially to an LC AOS. NCSR uses image nonlocal self-similarity and sparsity to improve the quality of restored images. The performance of the proposed method is confirmed by the results of simulation and experiments with LC AOS. Simulation results show that, for different objects, the PSNRs of deblurred images by the traditional method are improved by around 10 dB, while those by the proposed method are improved by 15 to 20 dB. The SSIMs of the latter are also higher than those of the former. Additionally, this work studies the influence of weak noise and finds that the effects of the proposed method are always better than those of the traditional PD with increasing noise. Results with the LC AOS show that the highest spatial resolutions that can be clearly distinguished are 1.59× diffraction limitation with AO on, 1.41× diffraction limitation with the traditional PD, and 1.26× diffraction limitation with the proposed method. Both simulation and

Fig. 11 Experimental results with LC AOS: (a) focused image with AO off, (b) focused image with AO on, and (c) defocused image with AO on.

Fig. 12 Experimental results with PD: (a) focused image, (b) deblurred image with Tikhonov regularization, and (c) deblurred image with NCSR.

experimental results imply the effectiveness of the method, especially for noise reduction and detail preservation. The proposed method can be applied in various high-resolution imaging techniques such as ground-based telescopes and fluorescence microscopes, among many other fields.

Acknowledgments

This work was supported by the National Natural Science Foundation of China (Grant Nos. 11774342, 61475152, 11804336, and 11704377) and the Foundation of State Key Laboratory of Applied Optics, Changchun Institute of Optics, Fine Mechanics and Physics, Chinese Academy of Sciences.

References

1. H. W. Babcock, "The possibility of compensating astronomical seeing," *Publ. Astron. Soc. Pac.* **65**(386), 229–236 (1953).
2. M. J. Booth, "Adaptive optical microscopy: the ongoing quest for a perfect image," *Light Sci. Appl.* **3**(4), e165 (2014).
3. R. A. Gonsalves and R. Chidlaw, "Wavefront sensing by phase retrieval," *Proc. SPIE* **207**, 32–39 (1979).
4. R. G. Paxman, B. J. Thelen, and J. H. Seldin, "Phase-diversity correction of turbulence-induced space-variant blur," *Opt. Lett.* **19**(16), 1231–1233 (1994).
5. N. Miyamura, "Test results of optimal phase diversity selection using a LCOS-SLM for remote sensing adaptive optics," *Proc. SPIE* **7723**(1), 772308 (2010).
6. R. A. Gonsalves, "Phase retrieval and diversity in adaptive optics," *Opt. Eng.* **21**(5), 829–832 (1982).
7. D. Wilding et al., "Phase diversity based object estimation in light-sheet fluorescence microscopy," in *OSA Technical Digest*, paper BoTu2A.2 (2017).
8. R. G. Paxman and J. R. Fienup, "Optical misalignment sensing and image reconstruction using phase diversity," *J. Opt. Soc. Am. A* **5**(5), 914–923 (1988).
9. C. Robert et al., "Improvement of phase diversity algorithm for non-common path calibration in extreme AO context," *Proc. SPIE* **7015**, 70156A (2008).
10. N. Védrenne et al., "Laser beam complex amplitude measurement by phase diversity," *Opt. Express* **22**(4), 4575–4589 (2014).
11. R. J. Noll, "Zernike polynomials and atmospheric turbulence," *J. Opt. Soc. Am.* **66**(3), 207–211 (1976).
12. C. R. Vogel and R. J. Plemmons, "Fast algorithms for phase-diversity-based blind deconvolution," *Proc. SPIE* **3353**(2), 994–1005 (1998).
13. B. J. Thelen et al., "Maximum a posteriori estimation of fixed aberrations, dynamic aberrations, and the object from phase-diverse speckle data," *J. Opt. Soc. Am. A* **16**(5), 1016–1025 (1999).
14. M. G. Löfdahl and G. B. Scharmer, "Wavefront sensing and image restoration from focused and defocused solar images," *Astron. Astrophys. Suppl. Ser.* **107**(2), 243–264 (1994).
15. D. J. Lee et al., "Evaluation of least-squares phase-diversity technique for space telescope wave-front sensing," *Appl. Opt.* **36**(35), 9186–9197 (1997).
16. R. G. Paxman, "Phase-diverse speckle reconstruction of solar data," *Proc. SPIE* **2302**, 268–280 (1994).
17. A. Capozzoli, G. D'Elia, and O. M. Bucci, "Regularizing strategy for image restoration and wave-front sensing by phase diversity," *J. Opt. Soc. Am. A* **16**(7), 1759–1768 (1999).
18. S. Zhang, B. Wang, and J. Zhao, "High resolution optical image restoration for ground-based large telescope using phase diversity speckle," *Optik* **125**(2), 861–864 (2014).
19. A. N. Tikhonov, "On the stability of inverse problems," *Dolk. Akad. Nauk SSSR* **39**(5), 176–179 (1943).
20. K. Dabov et al., "Image denoising by sparse 3-D transform-domain collaborative filtering," *IEEE Trans. Image Process.* **16**(8), 2080–2095 (2007).
21. H. Yu et al., "Analysis and reduction of errors caused by Poisson noise for phase diversity technique," *Opt. Express* **24**(19), 22034–22042 (2016).
22. W. Dong, L. Zhang, and G. Shi, "Centralized sparse representation for image restoration," in *Proc. of IEEE Conf. on Computer Vision*, pp. 1259–1266 (2011).
23. W. Dong et al., "Nonlocally centralized sparse representation for image restoration," *IEEE Trans. Image Process.* **22**(4), 1620–1630 (2011).
24. P. G. Zhang et al., "Hybrid particle swarm global optimization algorithm for phase diversity phase retrieval," *Opt. Express* **24**(22), 25704–25717 (2016).
25. A. Blanc, L. M. Mugnier, and J. Idier, "Marginal estimation of aberrations and image restoration by use of phase diversity," *J. Opt. Soc. Am. A* **20**(6), 1035–1045 (2003).
26. Z. Wang et al., "Image quality assessment: from error visibility to structural similarity," *IEEE Trans. Image Process.* **13**(4), 600–612 (2004).
27. Z. Xu et al., "Visible light high-resolution imaging system for large aperture telescope by liquid crystal adaptive optics with phase diversity technique," *Sci. Rep.* **7**(1), 10034 (2017).

Daosheng Wu received his BS degree in optical information science and technology from the Northwestern Polytechnical University in 2014. His dissertation research focused on liquid crystal adaptive optics systems with phase diversity technique. He is a doctoral student of the University of Chinese Academy of Sciences and studying in the State Key Laboratory of Applied Optics, Changchun Institute of Optics, Fine Mechanics and Physics, Chinese Academy of Sciences.

Biographies of the other authors are not available.